



ISSN: 2350-0328

**International Journal of Advanced Research in Science,  
Engineering and Technology**

**Vol. 8, Issue 11, November 2021**

# **Lead Doped Cadmium Ferrite for Radiation Protection**

**S. M. Mahmoud, A. M. Abdel Reheem, H. M. El-Sayed, H. El-Khabeary**

Accelerators & Ion Sources Department, Nuclear Research Center, Egyptian Atomic Energy Authority P.N. 13759, Cairo, Egypt.

Radiation Physics Department, National Center for Radiation Research and Technology  
Egyptian Atomic Energy Authority, P.N. 11787, Cairo, Egypt.

Physics Department, Faculty of Science, Ain Shams University.

Accelerators & Ion Sources Department, Nuclear Research Center, Egyptian Atomic Energy Authority P.N. 13759, Cairo, Egypt.

**ABSTRACT:** In the present work, spinel ferrite nanoparticles with composition  $Pb_xCd_{(1-x)}Fe_2O_4$ ;  $X=(0,0.2,0.4,0.6)$  was successfully synthesized by using hydrothermal process. Structural, surface morphology and magnetic properties were characterized by using XRD, TEM micrograph, SEM techniques, and VSM, respectively. The mass attenuation coefficient and the half value thicknesses for synthesized samples are measured using  $^{60}Co$  and  $^{137}Cs$  gamma sources. The composition  $Pb_{0.6}Cd_{0.4}Fe_2O_4$  showed recorded high mass attenuation in energy lines 0.662, 1.17, and 1.32 MeV, and so lowest half-value thickness. Also, the mass attenuation coefficient for the synthesized NPs materials is calculated by using MicroShield v5 (5.03-00056) software, a good agreement between theoretical calculations and experimental investigations was found.

**KEY WORDS:** Nanoparticles, Spinel Ferrite, Magnetic Properties, Mass attenuation, shielding properties.

## **I. INTRODUCTION**

Magnetic spinel ferrite nanoparticles, are materials with formula  $MFe_2O_4$ , they are chemically and thermally stable materials. They exhibit their importance from their wide applications in our life like, magnetic data storage, magnetic devices, water purifications, cancer therapy, gas sensors and industrial fields [1-7]. A variety of methods such as hydrothermal, sol-gel, and co-precipitation have been used to synthesize ferrite materials. Each method has unique advantages; hydrothermal synthesis is defined by Yshimura as the reactions occurring under conditions of high temperature and high pressure in aqueous solutions in a closed system [8]. Advantages of the hydrothermal method over other types of crystal growth are the ability to create crystalline phases. Also, it is suitable for growth of good-quality crystals with high melting point at low temperature. But the disadvantages of this method include the need for expensive autoclaves [9], take more time by comparing with other methods, and produced a small amount of ferrite nanoparticle according to the volume of the autoclave. Shielding materials are used to protect humans from hazards of ionizing radiation should be characterized by their high thermal and chemical stability, high corrosion resistance, and small half value thickness (HVL) of the material. The similarity between properties of shielding materials and ferrite leads to be used as shielding material for different types of ionizing radiation or even by mixing it with the most common shielding materials like concrete or cement to improve its shielding properties. Also, it can be mixed with a polymer material to be used in radiation protection products and can be used as sensor in the radiation field. It is well known that Pb is one of the most important materials for gamma-ray radiation protection and cadmium is a good absorber for thermal neutrons. Therefore, in this work; the Pb-doped Cd-ferrite nanomaterial is synthesized, characterized, and investigated to be used as a double shielding material for radiation protection products and gamma shielding.

## **II. EXPERIMENTAL DETAILS**

### **Materials:**

Chemicals that are used in ferrite NPs synthesis are ferric nitrate ( $Fe(NO_3)_3$ ), Lead nitrate ( $Pb(NO_3)_2$ ), Cadmium nitrate ( $Cd(NO_3)_2$ ), and Sodium hydroxide Pellets ( $NaOH$ ). All used chemicals have purity  $> 99\%$ .

**Synthesis of ferrite nanoparticle materials.**

The Hydrothermal method is used for synthesis the spinel ferrite NPs with composition  $Pb_xCd_{(1-x)}Fe_2O_4$ ,  $x=(0,0.2,0.4,0.6)$ . Stoichiometric amounts of the metal salts and sodium hydroxide were dissolved separately in 90ml of distilled water for the hydrolysis reaction. The salt solutions are mixed and the resultant mixture take places inside the autoclave Teflon lined. The autoclave is kept at 180°C for 18 hrs, and then the solution is washed many times. The precipitate powders are dried at 95°C then sintered at 500°C for 4 hrs.

**Characterization of ferrite NPs**

In this work the crystal structure of ferrite NPs have been identified by applying a completely computerized X-ray diffractometer (XRD), Shimadzu XRD-6000, at NCRRT, Cairo, Egypt [10,11] the surface morphology of the ferrite samples are studied by using Scanning Electron Microscopy (SEM) ZEISS, EVO-MA10 [12] Eventually, Fourier Transform Infrared absorption spectrum (FTIR) is an important contribution enabling identification of chemical functional groups corresponding to the synthesized ferrite NPs. A Transmission Electron Microscope (TEM) is used for recording high magnification images of samples [13].

**Gamma ray shielding property for ferrite NPs**

$^{60}Co$  and  $^{137}Cs$  gamma sources and Sodium iodine detector were used to investigate gamma-ray shielding property for synthesized NPs materials.

**III. RESULTS AND DISCUSSION**

**Characterization of nanoparticles ferrite materials.**

In this section different technics are used to characterization the spinel ferrite NPs with composition  $Pb_xCd_{(1-x)}Fe_2O_4$ ,  $x=(0,0.2,0.4,0.6)$ .

**XRD analysis**

Ferrite NPs have been characterized by using the X-ray diffractometer. The mean crystallite size D was calculated according to Scherer's equation [14].

$$D = 0.9 \lambda / (\beta \cos\theta) \tag{1}$$

where  $\beta$  is the full width at half maximum (FWHM) of the most intense peak. The experimental lattice constant for a cubic system was determined from the inter-planar spacing (d) by using this relation

$$a = d_{hkl} (h^2 + k^2 + l^2)^{1/2} \tag{2}$$

Where h, k, and l are the Miller indices of the diffraction peaks (hkl). The lattice strain was calculated by using the Williamson equation [15].

$$\epsilon = \beta / 4 \tan\theta \tag{3}$$

XRD patterns of  $Pb_xCd_{(1-x)}Fe_2O_4$   $x=(0,0.2,0.4,0.6)$  are shown in figure 1. It is observed that the formed samples have single-phase structure. The detected peaks are indexed to their corresponding (h k l) [16,17].

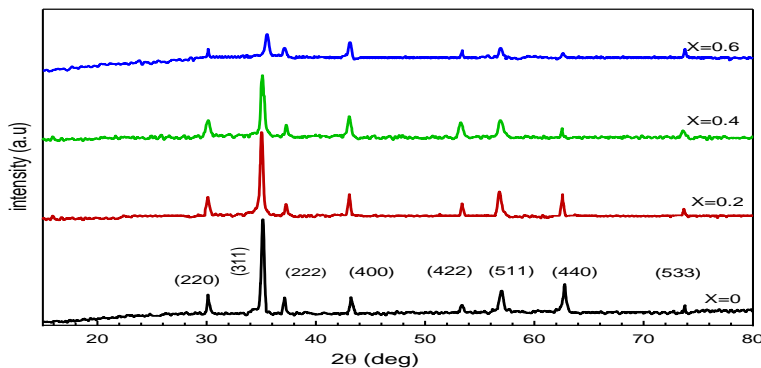


**Fig. (1). XRD patterns of  $Pb_xCd_{(1-x)}Fe_2O_4$ ;  $X=(0,0.2,0.4,0.6)$  ferrite NPs .**

Figure (2) shows the effect of Pb-content (x) on the lattice parameter. It is clear that, for  $x \leq 0.2$ , the lattice parameter increases with increasing Pb-content, this could be explained in terms of replacement of a large ionic radius of  $Pb^{2+}$  ion ( $1.33\text{\AA}$ ) instead of  $Cd^{2+}$  ion which has a smaller ionic radius ( $0.92\text{\AA}$ ). The decrease of lattice parameter for  $x > 0.2$  samples could be explained in terms of the solubility limit of Pb ions where the excess of Pb is segregated at the grain boundaries which cause compression on the lattice unit causing a decrement in the lattice parameter.

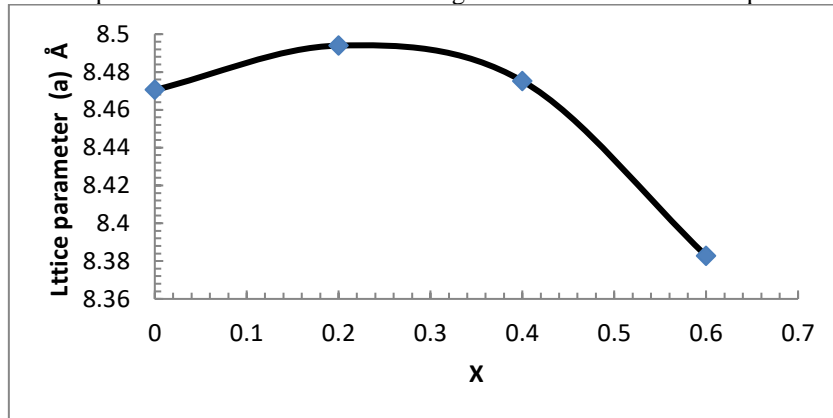


**Fig. (2). Lattice parameter variation with x for  $Pb_xCd_{(1-x)}Fe_2O_4$   $x=(0,0.2,0.4,0.6)$ .**

**The crystallite size and strain.**

The Williamson-Hall plots for  $Pb_xCd_{(1-x)}Fe_2O_4$   $x=(0,0.2,0.4,0.6)$  ferrite NPs as shown in figure 3. The slope of the linear fit of W-H plot represents the microstrain for the sample while the intercept represents its crystal size, also the negative slope indicates to the samples are compressed, but the positive slope indicates to the samples are under expansion [15, 18]. Figure (4) shows the effect of Pb content on both the crystalline size and the microstrain. We observed that the mean crystallite size ( $D_{W-H}$ ) ranged between 20 nm to 43 nm. Furthermore, the microstrain decreasing with increasing Pb content up to  $x=0.2$  then increase for  $x=0.4$  and further increases with  $x=0.6$ .

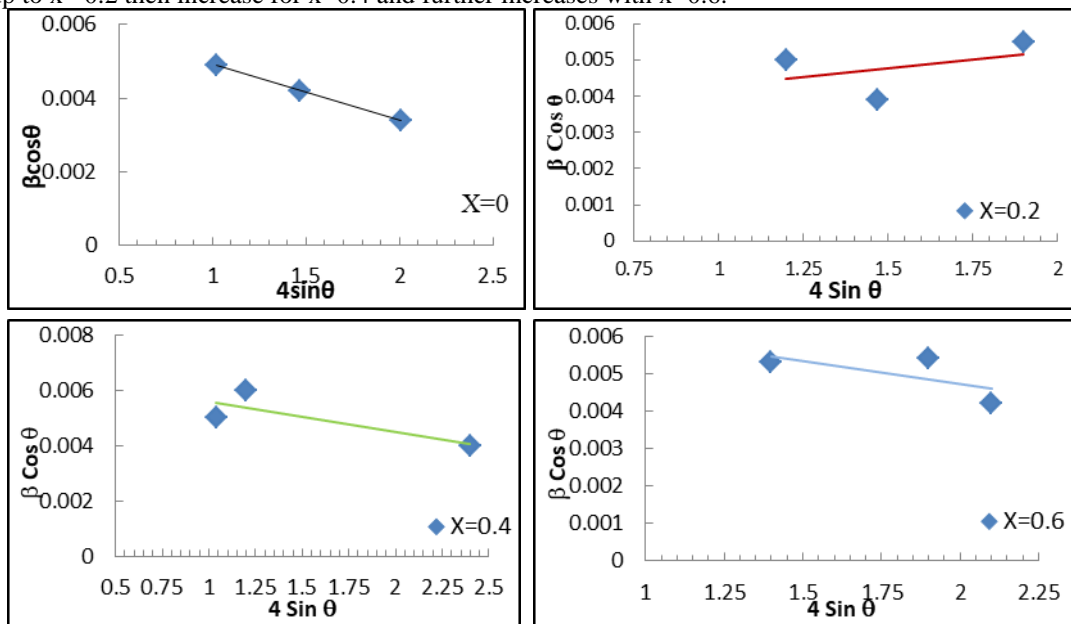


**Fig. (3) W-Hplots for  $Pb_xCd_{(1-x)}Fe_2O_4$ , ( $x=0,0.2,0.4,0.6$ )**

This could be attributed to the solubility limit of lead then the excess remains at the grain boundaries which causes the increase of the microstrain and sudden decrease in crystal size.

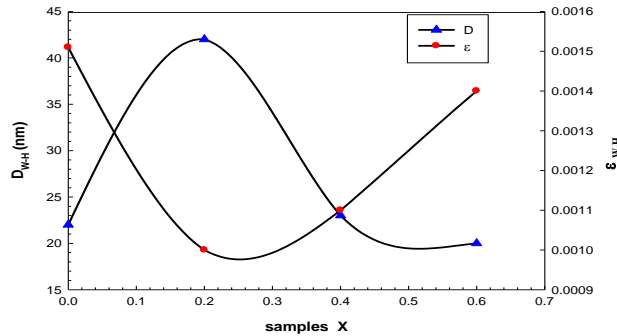


**Fig. (4).** the Variation of crystallite size and strain with x.

**Fourier Transform Infrared Spectroscopy (FTIR)**

Fourier Transform Infrared absorption spectrum is used to investigate the cation distribution of ferrites samples [19]. The FTIR spectrum of the investigated samples is shown in Figure (5) and the absorption bands are tabulated in the table (1). It is clear that the position of  $\nu_1$  band, which represents the Fe-O vibrational mode in A site, decreases with the increase of Pb content. On the other hand, the position band  $\nu_2$ , which represents the Fe-O vibrational modes in B site decreases with increasing lead concentration. The changes of  $\nu_1$  and  $\nu_2$  with increasing Pb-content indicate that the  $Cd^{2+}$  ion occupies A-site and  $Pb^{2+}$  ion occupies the B-site. Therefore, the proposed cation distribution of the investigated samples is  $(Cd_{1-x}Fe_x)O [Pb_xFe_{2-x}]$ .

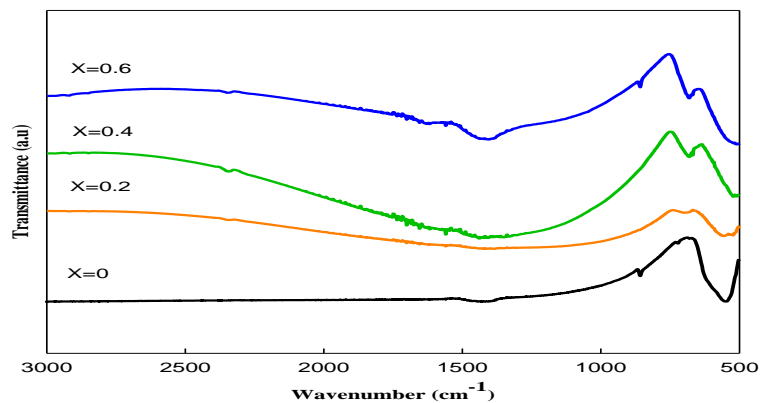


**Fig.(5).** FTIR spectra of  $Pb_xCd_{(1-x)}Fe_2O_4$   $x=(0,0.2,0.4,0.6)$  ferrite.

Table (1) .Two bands correlated to A & B sites for  $Pb_xCd_{(1-x)}Fe_2O_4$   $x=(0,0.2,0.4,0.6)$  ferrite NPs .

Lead Doped (x)	$\nu_1 (cm^{-1})$	$\nu_2 (cm^{-1})$
0	547	475
0.2	555	455
0.4	592	441
0.6	644	420

**Transmission Electron MICROSCOPE (TEM)**

The TEM images of  $Pb_x Cd_{(1-x)} Fe_2O_4$   $x=(0,0.2,0.4,0.6)$  ferrite NPs are shown in figure 6, all particles have a spherical shape and homogenous particle size-The particle size was labeled on each figure- in which the particle size increase with increasing Pb -content at  $x = 0,0.2$ . The dramatic decrease in the particle size for a sample with  $x=0.6$  could be attributed to the presence of Pb on the grain boundaries which prevents the crystal growth of the ferrite sample which agrees with XRD and strain values.

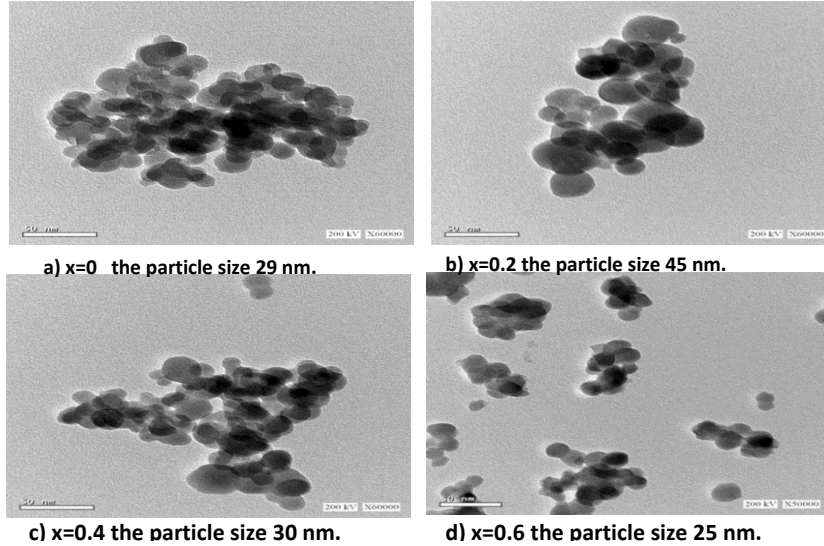


Fig. (6) TEM micrograph for  $Pb_xCd_{(1-x)}Fe_2O_4$   $x=(0,0.2,0.4,0.6)$  ferrite NPs .

### Scanning Electron Microscope (SEM)

The morphology and shape of the synthesized nanomaterials are investigated using SEM images. As clear in figure (7) the samples are characterized by the presence of different spherical particles with agglomerated form and almost in equal size. The increase of the porous structure in sample  $x=0.6$  when compared with other samples is due to its small grain size and increasing of particles number on the effective area which causes more porous on the surface effective area [20, 21].

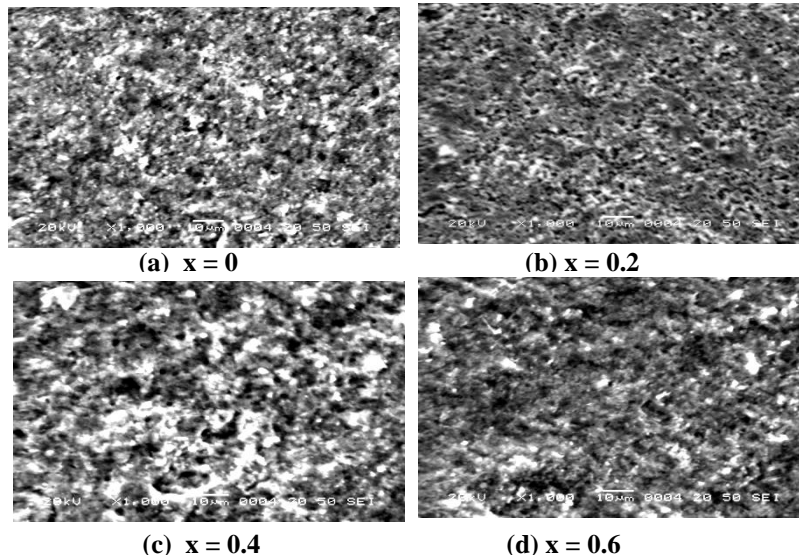
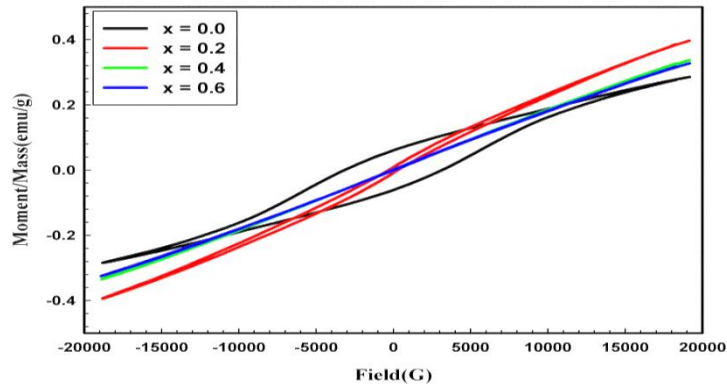


Fig. (7): Scan Electron Microscope (SEM )for  $Pb_xCd_{(1-x)}Fe_2O_4$   $x=(0,0.2,0.4,0.6)$  ferrite NPs .

### Magnetic Properties:

The Magnetic *hysteresis* loops for the investigated samples are shown in figure (8), the summary of the hysteresis parameters are tabulated in table 2. It is obvious that both samples ( $x=0$  &  $x=0.2$ ) have a hysteresis loop i.e. these samples have ferromagnetic behavior while for samples ( $x=0.4$  &  $x=0.6$ )  $H_c$  almost equal to zero i.e. it is superparamagnetic behavior. Furthermore increasing Pb content causes an increase in saturation magnetization for the sample ( $x=0.2$ ) then the magnetization decreases for the other samples. This could be explained in the light of the proposed cation distribution

(Cd<sub>1-x</sub> Fe<sub>x</sub>) O [Pb<sub>x</sub> Fe<sub>2-x</sub>]. For x=0, the ferrite is normal spinel structured i.e, all Fe<sup>3+</sup> ions are in B-site, the strong B-B interaction causes increase canting angle which makes this sample almost antiferromagnetic material. By increasing Pb-content, which is a nonmagnetic ion, in B site, the B-B interaction decreases so, it will decrease the canting angle causing the increase of magnetization. Further increase in the Pb content will dilute the magnetic moments in B site while the Fe<sup>3+</sup>ion increase in A site. Therefore, the difference between moments in B and A sites decreases causing the decrease of magnetization. The Presence of high H<sub>c</sub> for samples x=0 and x=0.2 could be explained in terms of the formation of Fe<sup>2+</sup> in B-site due to the high quantity of Fe ion in B- site which is responsible for magnetic anisotropy i.e. increasing H<sub>c</sub>[22].



**Fig. (8 ).M-H loops Pb<sub>x</sub> Cd<sub>(1-x)</sub> Fe<sub>2</sub>O<sub>4</sub>; x=(0,0.2,0.4,0.6)ferrite NPs .**

**Table: (2) Saturation magnetization (M<sub>s</sub>), remanence magnetization (M<sub>r</sub>) and coercivity (H<sub>c</sub>).**

Pb-content (x)	M <sub>s</sub> (emu/g)	M <sub>r</sub> (emu/g)	Coercivity (H <sub>ci</sub> ) G
0.0	0.195	6.08x10 <sup>-2</sup>	3148.8
0.2	0.288	8.52x10 <sup>-3</sup>	287.37
0.4	0.226	1.15x10 <sup>-3</sup>	65.076
0.6	0.233	1.04x10 <sup>-3</sup>	54.372

**Measurement of ferrite nanoparticles shielding property for Gamma-ray.**

Nanoparticles Ferrite samples with different composites Pb<sub>x</sub>Cd<sub>(1-x)</sub>Fe<sub>2</sub>O<sub>4</sub>; x=(0.0,0.2,0.4,0.6)were compressed at 5.5 tons as discs with diameter 13 mm. To investigate the shielding properties of our samples, <sup>60</sup>Coand <sup>137</sup>Cssources are used as gamma-ray sources with energy lines 1.17, 1.33, and 0.662 MeV.The sample is located at 4.5cm distance from the cobalt and cesium sources and 12cm distance from the sodium iodide detector which operated with 540 kV ,and detectorplug with energy mode. The setup is surrounded by Lead blokes to avoid radiation hazards. NaI detector was connected to “Maestro” computerized software.

Linear and mass attenuation coefficient for NPs Ferrite samples were calculated by using the following relation;

$$I=I_0 e^{-\mu h}= I_0 e^{-\mu/\rho (\rho h)}(4)$$

Where I and I<sub>0</sub> are intensities of gamma radiation transverse to sample and air respectively, μ is the linear attenuation coefficient, h is the distance traveled and μ/ρ is the mass attenuation coefficient.

The experimental measurements of linear, mass attenuation coefficient, and half value thicknesses for NPs Ferrite samples Pb<sub>x</sub>Cd<sub>(1-x)</sub>Fe<sub>2</sub>O<sub>4</sub>x=(0,0.2,0.4,0.6)are shown in the figures 9&10.

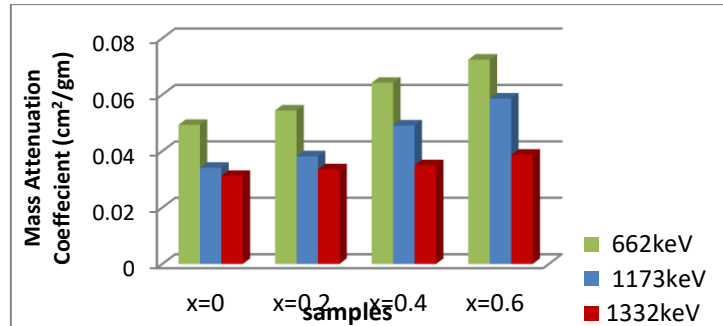


Fig. (9). Experimental mass attenuation coefficient variation with x of the synthesized samples.

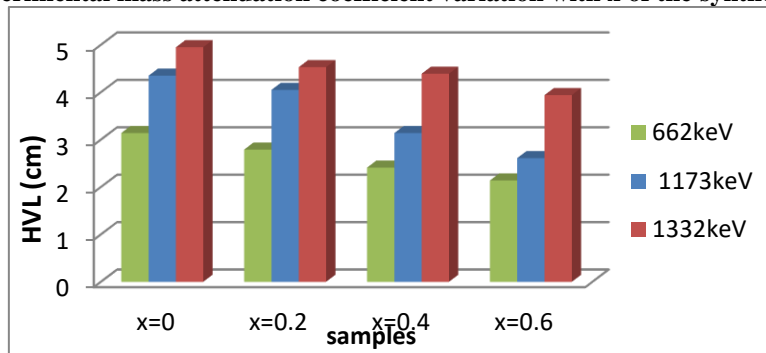


Fig. (10). Experimental half-value thickness (x<sub>1/2</sub>) variation with x of the synthesized samples

As clear in figures (9, 10) the mass attenuation coefficient for the synthesis of spinel ferrite NPs was increased with increasing Pb- content and the composition (x=0.6) records the maximum value of mass attenuation coefficient and so minimum HVL for (1.17, 1.33 and 0.662)MeV energy lines. The MicroShield v5 (5.03-00056) software was used to calculate the theoretical Mass Attenuation coefficient for the synthesized powder at different values of gamma-ray energy.

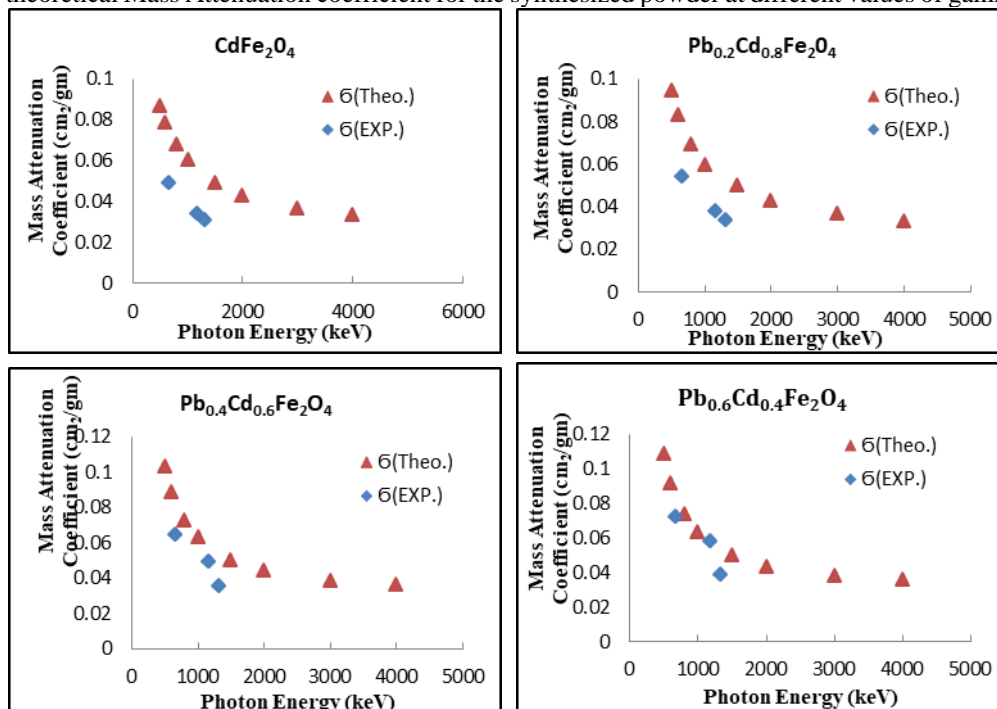


Fig.(11) Theoretical and experimental Mass attenuation coefficient of the investigated synthesizedNPs.



From figure (11) the agreement between theoretical and experimental mass attenuation coefficient increases with increasing Pb-content, this could be due to the Pb is the main absorber material for gamma radiation, in which for sample  $x=0.6$  the mass attenuation coefficient was recorded value equals  $0.05861 \text{ cm}^2/\text{gm}$  at  $1.173 \text{ MeV}$  gamma energy line.

#### IV. CONCLUSION

$\text{Pb}_x\text{Cd}_{(1-x)}\text{Fe}_2\text{O}_4$ ;  $x=(0,0.2,0.4,0.6)$  ferrite NPs are successfully synthesized by effective hydrothermal technique. The XRD and FTIR data indicated the presence of a cubic spinel phase. The particle size for this composition ranged from  $29 \text{ nm}$  to  $45 \text{ nm}$  while the crystal size  $D$  ranged between  $22 \text{ nm}$  and  $43 \text{ nm}$ . The synthesized materials exhibit a super paramagnetic properties for samples that have  $x=(0.4,0.6)$  and ferromagnetic properties for  $x=0$  and  $x=0.2$ . The Coercivity ( $H_c$ ) is recorded high value for sample  $x=0$ . Synthesized NPs ferrite introduced a good contribution to be a successful gamma-ray shielding material for different gamma-ray energies. The composition ( $x=0.6$ ) is recorded the highest mass attenuation coefficient which reaches  $0.05861 \text{ cm}^2/\text{g}$  for  $1.173 \text{ MeV}$  photon energy and  $2.189 \text{ (cm)}$  half-value thickness. The composition with  $x=0.6$  is a suitable candidate as a gamma-ray shielding.

#### REFERENCES

- [1]. R. Bhattacharya, P. Mukherjee, Biological properties of “naked” metal nanoparticles, *Adv. Drug Deliv. Rev.* 60 (11) 12, 2008.
- [2]. Sun, H. T.; Cantalini, C.; Faccio, M.; Pelino, M.,  $\text{NO}_2$  gas sensitivity of sol-gel-derived  $\alpha\text{-Fe}_2\text{O}_3$ , *Thin Solid Films*, 269, 97, 1995.
- [3]. Chakrabarti, S.; Mandal, S. K.; Chaudhuri, S. Cobalt doped  $\text{Fe}_2\text{O}_3$  nanoparticles: Synthesis and magnetic properties. *Nanotechnology*, 16, 506–511, 2005.
- [4]. J. Liao, T. Qi, B. Chu, J. Peng, F. Luo, and Z. Qian, Multifunctional nanostructured materials for multimodal cancer imaging and therapy. *J. Nanosci. Nanotech.* 14, 175, 2014.
- [5]. Darshane, S. L.; Deshmukh, R. G.; Suryavanshi, S. S. Gas-sensing properties of zinc ferrite nanoparticles synthesized by the molten-salt route. *J. Am. Ceram. Soc.*, 91, 2724–2726, 2008.
- [6]. L.A. Frolova, A.A. Pivovarov, T.E. Butyrina, E.G. Tsepich, Purification of Wastewaters, Containing Chromium, by a Sorbent Based on Blast Furnace Slag, *J Water Chem Techno*, 37, 4, 2015. <https://doi.org/10.3103/S1063455X15040062>.
- [7]. A. S. Awed, M. I. A. Abdel Maksoud, M. M. Atta, Ramy Amer Fahim. Nonlinear optical properties of irradiated 1,2-dihydroxyanthraquinone thin films: merged experimental and TD-DFT insights, *Journal of Materials Science: Materials in Electronics* 30:7858–7865, 2019. <https://doi.org/10.1007/s10854-019-01105-6>.
- [8]. Byrappa K, Yoshimura M, *Handbook of hydrothermal technology*. Noyes Publications, NJ, USA, 2001.
- [9]. O'Donoghue, M., *A guide to Man-made Gemstones*. Great Britain: Van Nostrand Reinhold Company, pp. 40, 1983. ISBN 0-442-27253-7.
- [10]. A.M. Reheem, M.A. Maksoud, A. Ashour, Surface modification and metallization of polycarbonate using low energy ion beam, *Radiat. Phys. Chem.* 125, 171–175, 2016.
- [11]. A.M. Reheem, A. Atta, M.A. Maksoud, Low energy ion beam induced changes in structural and thermal properties of polycarbonate, *Radiat. Phys. Chem.* 127, 269–275, 2016.
- [12]. A.I. El-Batal, G.S. El-Sayyad, A. El-Ghamry, K.M. Agaypi, M.A. Elsayed, M. Gobara, Melanin-gamma rays assistants for bismuth oxide nanoparticles synthesis at room temperature for enhancing antimicrobial, and photocatalytic activity, *J. Photochem. Photobiol. B Biol.* 173, 120–139, 2017.
- [13]. Z. Zhu, R. Gonthier, L. neirinck, High-performance liquid chromatography-mass spectrometry method for determination of anagrelide in human plasma, *Journal of Chromatography B*, 822 (1-2) 238–243, 2005.
- [14]. H. El Moussaoui, et. al., Experimental studies of neodymium ferrites doped with three different transition metals, *Mater. Lett.* 171, 142–145, 2016.
- [15]. Williamson G K & Hall W H, X-Ray Line Broadening From Filled Aluminum And Wolfram, *Acta Metal.*, 1, 22, 1953. [https://doi.org/10.1016/0001-6160\(53\)90006-6](https://doi.org/10.1016/0001-6160(53)90006-6).
- [16]. M. I. A. Abdel Maksoud, et. al., Tunable structures of copper substituted cobalt nanoferrites with prospective electrical and magnetic applications, *Jou. of Materials Science: Materials in Electronics*, 30, 4908, 2019. <https://doi.org/10.1007/s10854-019-00785-4>.
- [17]. M.N. Akhtar, A.B. Sulong, M. Ahmad, M.A. Khan, A. Ali, M. Islam, Impacts of Gd–Ce on the structural, morphological and magnetic properties of garnet nanocrystalline ferrites synthesized via sol–gel route, *J. Alloys Compd.* 660, 486–495, 2016.
- [18]. W. H. Hall, X-ray line Broadening in metals, *Proc. Phys. Soc. (London)*, A 62, 741, 1949.
- [19]. M. Amer, A. Matsuda, G. Kawamura, R. El-Shater, T. Meaz, F. Fakhry, Characterization and structural and magnetic studies of as-synthesized  $\text{Fe}_2^+\text{Cr}_x\text{Fe}_{(2-x)}\text{O}_4$  nanoparticles, *Journal of Magnetism and Magnetic Materials*, 439, 373, 2017.
- [20]. E. El-Ghazzawy, M. Amer ; Structural, elastic and magnetic studies of the as-synthesized  $\text{Co}_{1-x}\text{Sr}_x\text{Fe}_2\text{O}_4$  nanoparticles, *Journal of Alloys and Compounds*, 690, 293–303, 2017. <https://doi.org/10.1016/j.jallcom.2016.08.135>.
- [21]. S. M. Ismail, Sh. Labib, and S. S. Attallah; Preparation and characterization of nano-cadmium ferrite, *Journal of Ceramics Journal of Ceramics*, vol. 2013, Article ID 526434, 8 p., 2013. <https://doi.org/10.1155/2013/526434>.
- [22]. M. A. Ashmawy, A. A. Sattar and H. M. El-Sayed; Microstructure effect on the structural, interfacial and magnetic properties of particulate composite and 0-3 core shell composite, *Journal of Physics: Conf. Series* 1253, 012017, 2019.